High-temperature continuous hydrothermal post treatment derived g-C$_3$N$_4$ for enhanced photocatalytic H$_2$ production

Binjiang Zhai[a, 1], Yi Li[a, 1], Yuzhou Jiang[a, b], Liuhao Mao[a], Jinwen Shi[a, *], Qiangqiang Zhao[a], Zhongda Bin[a], Fanyu Wang[a], Yanping Du[c, *], Hui Jin[a, *]

a   International Research Center for Renewable Energy, State Key Laboratory of Multiphase Flow in Power Engineering, Xi'an Jiaotong University, Xi'an 710049, China.

b   Huaneng Shaanxi Power Generation Co., Ltd, Xi'an 710075, China.

c   School of Engineering, Lancaster University, Lancaster LA1 4YW, UK.

*   Corresponding authors.

     E-mail addresses: jinwen_shi@mail.xjtu.edu.cn (J, Shi), jinhui@mail.xjtu.edu.cn (H. Jin), y.du17@lancaster.ac.uk (Y. Du).

1   These authors contributed equally.

Abstract: Nowadays, hydrothermal post treatment is a promising method for the modification of g-C_3N_4. This paper illustrates the post-treatment modification of g-C_3N_4 achieved by using a continuous hydrothermal system (CHS) with high heating rates (25-50°C/s), short residence time (25.2-50.3 s), high reaction temperatures (250-300°C) and high pressure (about 19 MPa). The continuous hydrothermal post treatment derived g-C_3N_4 (CHT-CN) prepared at 280°C with 9 ml min^{-1} flow rate of g-C_3N_4 dispersion (CN-280/9) exhibits 5.6 times the photocatalytic H_2-evolution activity of CN-30/9 under visible light irradiation ($\lambda > 400$ nm). Due to the exfoliation and shearing action of high-temperature and high-pressure water, the specific surface area of CN-280/9 reaches 65.8 m^2 g^{-1}, which is 4.3 times of CN-30/9 and therefore lead to an increase in reactive sites available for photocatalytic reactions. Moreover, the continuous hydrothermal post treatment results in the disruption of the conjugate structure of pristine g-C_3N_4 to build new channels, which allows more electrons to be transferred from bulk to surface to participate in the reduction reaction, and thus enhancing the H_2-evolution activity. This work provides a valuable reference to potentially achieving the large-scale production of efficient photocatalysts based on the continuous high-temperature and high-pressure hydrothermal method.

Keywords: continuous system, graphitic carbon nitride, hydrogen, hydrothermal synthesis, solar energy

1. Introduction

Solar energy is abundant and widely distributed, but its application is limited by instability, discontinuity and low energy density. Photocatalytic hydrogen production has the potential to transform solar energy into clean and pollution-free hydrogen energy, which shows promise in fundamentally initiating a change to the current environmental crisis and energy deficiency. Since the discovery by Fujishima and Honda in 1972 that TiO_2 can decompose water to produce hydrogen under light irradiation [1], numerous catalysts, such as metal oxides (TiO_2 [2, 3], ZnO [4], CeO_2 [5]), metal nitrides (GaN [6], AlN [7]), metal sulfides (CdS [8], PdS [9], MoS_2 [10]), non-metallic compounds (Graphite carbon nitride [11, 12], covalent-organic-framework material [13, 14]), have been found for photocatalytic hydrogen production. However, most of photocatalysts face problems such as low efficiency, instability and high cost. It is imperative to enhance the synthesis process to develop photocatalysts that are more efficient and cost-effective.

Graphitic carbon nitride (g-C_3N_4) is a kind of layered n-type organic polymer semiconductor with triazine ring (C_3N_3) or 3-s-triazine ring (C_6N_7) as basic structure, and the layers are held together by van der Waals force. In 2009, Wang's team discovered g-C_3N_4 for using in photocatalytic hydrogen production [15], which garnered significant attention from the academic community [16-18]. However, most of the reported bulk g-C_3N_4 was synthesized via thermal polymerisation, leading to low specific surface area and therefore poor photocatalytic activity [19, 20]. Currently, various post-treatment methods were reported to enhance the photocatalytic activity of g-C_3N_4, such as thermal treatment [21-23], hydrothermal/solvothermal treatment [24], plasma treatment [25, 26]. Among these, hydrothermal post treatment has gained much attention due to its eco-friendliness, easy operability and scalability.

Hao and his research team proposed hydrothermal post-treatment method of g-C_3N_4 in 2016 [24]. After an 8 h's hydrothermal process at 190°C, modified g-C_3N_4 presented well enhanced photocatalytic efficiency due to small particle size, large specific surface area and low interfacial charge transfer resistance. Besides, the application of acid [27-29] and alkaline [30, 31] solutions to hydrothermal treatment, or the use of organic solvents for solvothermal treatment [32, 33], is now a widespread practice in post treatment of g-C_3N_4. In fact, g-C_3N_4 is susceptible to oxidation at high hydrothermal temperatures, and therefore most of post-treatment methods of g-C_3N_4 are conducted at temperatures below 200°C [34-36]. In our recent researches, a rapid high-temperature hydrothermal post treatment [37] and a supercritical CH_3OH posttreatment strategy [38] for g-C_3N_4 was realized by using the homemade

3

70 microreactor. These methods greatly reduced the reaction time and substantially enhanced the

71 H_2-evoluation rate of modified g-C_3N_4, which displayed 5.1 times and 7.2 times H_2-evolution

72 rate compared to bulk g-C_3N_4 under visible-light irradiation ($\lambda > 400$ nm), respectively.

73 However, with the increase of reaction temperature and residence time, both the yield and the

74 H_2-evoluation rate of g-C_3N_4 decreased, which may be attributed to the destruction of the g-

75 C_3N_4 crystal structure caused by the prolonged high-temperature reaction. As the temperature

76 and pressure increased, the physicochemical properties, such as density, viscosity,

77 electronegativity, polarity, ion-product constant, of fluid would undergo significant changes.

78 Thus, high treatment temperature and high heating rate are two crucial factors for efficient g-

79 C_3N_4 modification and avoiding the excessive decomposition of g-C_3N_4. All the mentioned

80 solvothermal treatments were performed in a batch reactor, which made them inadequate in

81 terms of heating rates.

82 Based on this consideration, the continuous hydrothermal system (CHS) is considered as an

83 effective method for significantly increasing heating rates through strong heat transfer via

84 instantaneously mixing high-temperature water and low temperature solutions. Moreover, the

85 continuous hydrothermal process offers the advantages of short residence time, scalability, and

86 intense heat and mass transfer processes. Therefore, continuous hydrothermal technology has

87 been widely applied, with notable instances, including the work of Tadafumi Adschiri and

88 Jawwad A. Darr, who employed a CHS to produce nanomaterials (ZnO [39], $MgFe_2O_4$ [40] and

89 $NiCo_2O_4$ [41]). Our research group has also made use of continuous supercritical hydrothermal

90 system, investigating hydrogen production via coal gasification [42, 43].

91 In this work, a CHS was used for post treatment of g-C_3N_4, and a visualized batch hydrothermal

92 treatment was also conducted to observe the reaction process of g-C_3N_4 at high temperatures.

93 The g-C_3N_4 dispersion was instantly heated by mixing with preheated water of high temperature

94 above 300ºC and then subjected to high-temperature hydrothermal treatment in the CHS. The

95 high treatment temperature, high heating rate and short residence time can prevent the over-

96 decomposition of g-C_3N_4 and significantly enhance the photocatalytic H_2-evolution rate of

97 continuous hydrothermal post treatment derived g-C_3N_4 (CHT-CN). Furthermore, the

98 mechanism of the enhanced photocatalytic activity was investigated based on several

99 characterization methods.

100

101 **2. Experimental Methods**

102 **2.1. Chemicals**

103   Melamine ($C_3H_6N_6$) and triethanolamine (TEOA, $C_6H_{15}NO_3$) were purchased from Sinopharm

104   Chemical Reagent Co., Ltd. The aqueous solution with an equivalent Pt content of 0.7934

105     $mg \cdot mL^{-1}$ was prepared by using chloroplatinic acid hexahydrate ($H_2PtCl_6 \cdot 6H_2O$) purchased

106   from Sigma Aldrich Co., Ltd, and was used for the loading of metallic Pt as co-catalyst. Argon

107   (Ar) gas (99.999%) was purchased from Shaanxi Xinghua Group Co., Ltd. Deionized water

108   with a resistivity of 18.25 MΩ cm was used in the experiments. All the reagents were analytical

109   reagents and were used without any further purification.

110   **2.2. Preparation of pristine g-C_3N_4**

111   Melamine (10 g) was added to a covered ceramic crucible, then calcined in a muffle furnace

112   under an air atmosphere at 550°C for 4 h with a ramping rate of 5°C/min from room temperature

113   to 550°C. The resulting powder were ground and designated as CN.

114   **2.3. Visualized batch hydrothermal post treatment of g-C_3N_4**

115   To observe the change of g-C_3N_4 in a high-temperature hydrothermal process at autogenous

116   pressure, visualized batch hydrothermal experiment was carried out using a quartz tube with an

117   internal volume of 1.0 mL. Initially, a 5 $mg \cdot mL^{-1}$ g-C_3N_4 dispersion was prepared with

118   deionized water and stirred to prevent g-C_3N_4 particles from precipitation. Next, 0.2 mL of the

119   dispersion was injected into the quartz tube, which was then sealed using a hydrogen flame gun.

120   Finally, the quartz tube was put in a preheated sand bath at a specified temperature for a

121   specified period of minutes, and then was taken out and cooled to room temperature in air.

122   **2.4. Continuous hydrothermal post treatment of g-C_3N_4**

123   The continuous hydrothermal system (CHS) used in this work is shown in Fig. 1 and Fig. S1.

124   The high-pressure pumps (3, 4) and backpressure valve (9) permitted the application of elevated

125   pressure, which boosted the boiling point of the solution and decreased evaporation and thus

126   facilitated heat transfer in the pipeline. The whole hydrothermal post-treatment process mainly

127   included the steps of preheating, mixing, reaction, cooling and collection. Deionized water (2)

128   flowed through a preheater and mixed with the g-C_3N_4 dispersion (1) in a T-mixer (6) at first,

129   and then flowed immediately into the reactor (7) to complete the reaction, and then flowed

130   through a cooler (8) and a backpressure valve (9), and finally was collected in a storage tank

131   (10). Pump (3) with a flow rate (m_1) range of 0 to 20 $mL \cdot min^{-1}$ was used to pump g-C_3N_4

132   dispersion, and the flow rate was shown in real time. Pump (4) with a flow rate (m_2) range of 0

133   to 108 $mL \cdot min^{-1}$ was used to pump deionized water, and the flow rate was monitored by an in-

134   line flow meter. The reactor was a cylinder with an internal diameter of 14 mm and a height of

135   336 mm, and with a heating layer to ensure the target reaction temperature. Temperature and

136   pressure sensors were positioned with a distance of 84 mm vertically along the reactor to

137   provide real-time data. In addition, all pipes used in the system were made of SS316 with an

138   internal diameter of 4 mm.

139   The post-treatment process of g-C_3N_4 in the CHS was carried out as follows. Initially, the

140   operation parameters of the experimental system, such as flow rate, pressure and temperature,

141   were adjusted according to the experimental program. Subsequently, the g-C_3N_4 powder (3 g)

142   was dispersed in deionized water (600 mL), which was then stirred for 60 min and

143   ultrasonicated for 5 min for the well dispersion of g-C_3N_4 powder. The obtained dispersion was

144   then pumped into the CHS for high-temperature and high-pressure hydrothermal post treatment

145   for tens of seconds. Finally, the collected dispersion was filtered through filter membrane (0.20

146   μm), and then washed with water and then dried at 60°C for 12 h. The resulting samples were

147   named as CN-T/m_1, in which T represented reaction temperature and m_1 represented the flow

148   rate of Pump (3).
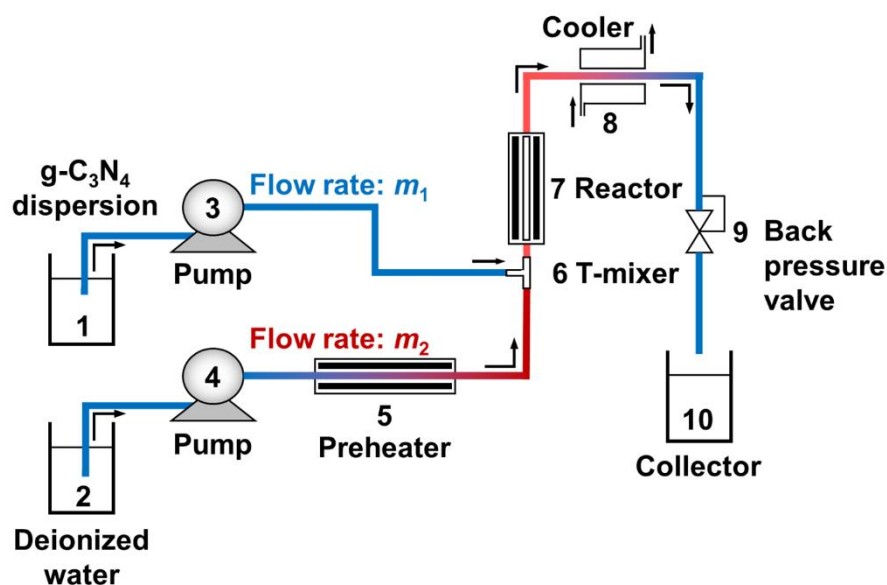
149

150   **Fig. 1.** Schematic diagram of the CHS.

151   **2.5. Photocatalytic performance measurement of samples**

152   Photocatalytic H_2-evolution measurements were carried out in a Pyrex glass reactor (105 mL),

153   using a Xe lamp (300 W) as the light source with visible-light irradiation after equipping with

154   a 400 nm cut-off filter. Photocatalyst (20 mg) was dispersed in 10 vol.% TEOA aqueous

155   solution (80 mL), and then H_2PtCl_6 aqueous solution containing 0.2 mg Pt was added into the

156   dispersion. The photocatalytic reactor was purged with Ar for 20 min to eliminate O_2 before

157   the photocatalytic reaction. During the measurement, the solution was maintained at 35 °C by

158   circulating water and was stirred constantly. The evolved gas was detected using a North Point

159   NP-GC-901A gas chromatograph (Ar as carrier gas, thermal conductivity detector (TCD),

160   TDX-01 column).

The apparent quantum yield (AQY) was measured under the irradiation of light with different wavelengths, i.e., 360, 380, 400, 420, 435, 450 and 475 nm realized by band-pass filters. The light intensities were recorded using a photoradiometer (PerfectLight, PL-MW 2000, China). The AQY values were obtained as follows.

$$AQY(\%) = \frac{\text{Number of evolved hydrogen molecules} \times 2}{\text{Number of incident photons}} \times 100\%$$

2.6. Characterization of samples

The characterizations of the photocatalysts were listed as follows. X-ray diffraction (XRD) patterns were obtained with a diffractometer (PANalytical X'pert MPD Pro, Netherlands) by a scan rate of $2°$ min^{-1} in the 2θ range from 10 to $80°$ under Ni-filtered Cu Kα irradiation (λ = 1.5406 Å). Ultraviolet-visible spectrophotometer (UV-Vis) were collected by a UV-Vis-near-IR spectrophotometer (Hitachi U-4100, Japan) with $BaSO_4$ reference in the range from 300 to 800 nm. All materials were degassed under vacuum at 423 K for 12 h. X-ray photoelectron spectroscopy (XPS) were recorded by an X-ray photoelectron spectroscope (Kratos Axis Ultra DLD, Japan) using a monochromatic Al Kα line source (hv = 1486.69 eV), and the adventitious C 1s peak at 284.8 eV was applied as reference. Fourier transform infrared spectra (FTIR) were recorded by a FTIR spectrophotometer (Bruker, Vertex 70, Germany) with using the KBr pellet technique. Brunauer-Emmette-Teller (BET) surface area measurements were recorded by an accelerated surface area and porosimetry analyzer (Micromeritics ASAP 2460, USA) with N_2 adsorption analysis, and pore volumes were calculated from desorption branches of N_2 adsorption-desorption isotherms by the Barrett–Joyner–Halenda (BJH) method. Transmission electron microscopy (TEM) images were obtained from a transmission electron microscope (FEI Tecnai G^2 F30 S-Twin, USA) with an accelerating voltage of 300 kV. Photoluminescence (PL) spectra and time-resolved photoluminescence (TRPL) spectra were obtained from a steady-state fluorescence spectrophotometer (PTI QuantaMaster 40, USA) at room temperature with an excitation wavelength of 337 nm. Scanning electron microscopy (SEM) images were carried out by a field-emission scanning electron microscope (JEOL JSM-7800F, Japan).

3. Results and Discussion

3.1. Influence factors of photocatalytic H$_2$-production performance

3.1.1. Exploration of the major parameters

Fig. 2a shows the results of the visualized batch hydrothermal post treatment of g-C$_3$N$_4$ with different heating temperatures and heating time. The quantity of solid residue after the hydrothermal reaction showed that the amount of g-C$_3$N$_4$ particles decreased with an increase

7

in heating temperatures and heating time, and the g-C_3N_4 was almost completely decomposed with a heating temperature of 320°C and heating time of 20 min in the quartz batch reactor. Similar to the batch hydrothermal treatment, the reaction temperature and residence time are also the main factors in continuous hydrothermal treatment of g-C_3N_4.

Computational Fluid Dynamics (CFD) were used to investigate the temperature distribution of T-mixer in CHS (Fig. 2b), and the actual hydrothermal process was also monitored in real-time (Fig. 2c) to verify the accuracy of the simulation by temperature sensors setting at Y = 0, 84, 168 and 252 mm (Fig. 2b) in T-mixer (6) and reactor (7). Fig. 2d shows the average surface temperature calculated from static temperature simulation (T_{ave}) and the real-time temperature (T_{real}) recorded from temperature sensors in CHS. At the position of Y = 84, 168 and 252 mm, there were no significant differences between T_{ave} and T_{real}, demonstrating that the simulation results well matched with the experimental data. Due to differences in density, flow rate and buoyance, the fluids moved concurrently inside the pipe with minimal mixing and maintained a relatively stable interface that was investigated as "fluid partitioning" by Lester et al [44]. around Y = 0 mm, where hence the large difference between T_{ave} (492.8 K) and T_{real} (531.5 K) appeared. It also could be observed from Fig. 2c that the real-time temperature curves at Y = 0 mm fluctuated significantly, indicating that the heat and mass transfer was more intense at the inlet of the T-mixer. As the mixed fluid flowed along the reactor (7), the colder g-C_3N_4 dispersion sunk into the preheated high-temperature water, and the temperature distribution of the cross-section was more uniform at Y = 84 mm, where the T_{ave} and T_{real} were 534.2 K and 540.0 K, respectively, with only a minor difference. Correspondingly, the real-time temperature curve at Y = 84 mm was similar to Y = 168 and 252 mm, and the fluctuations were significantly smaller than the curve at Y = 0 mm. The above analysis demonstrated that the mixing heating method used in CHS allowed the g-C_3N_4 dispersion to reach a high temperature in a very short period of time.
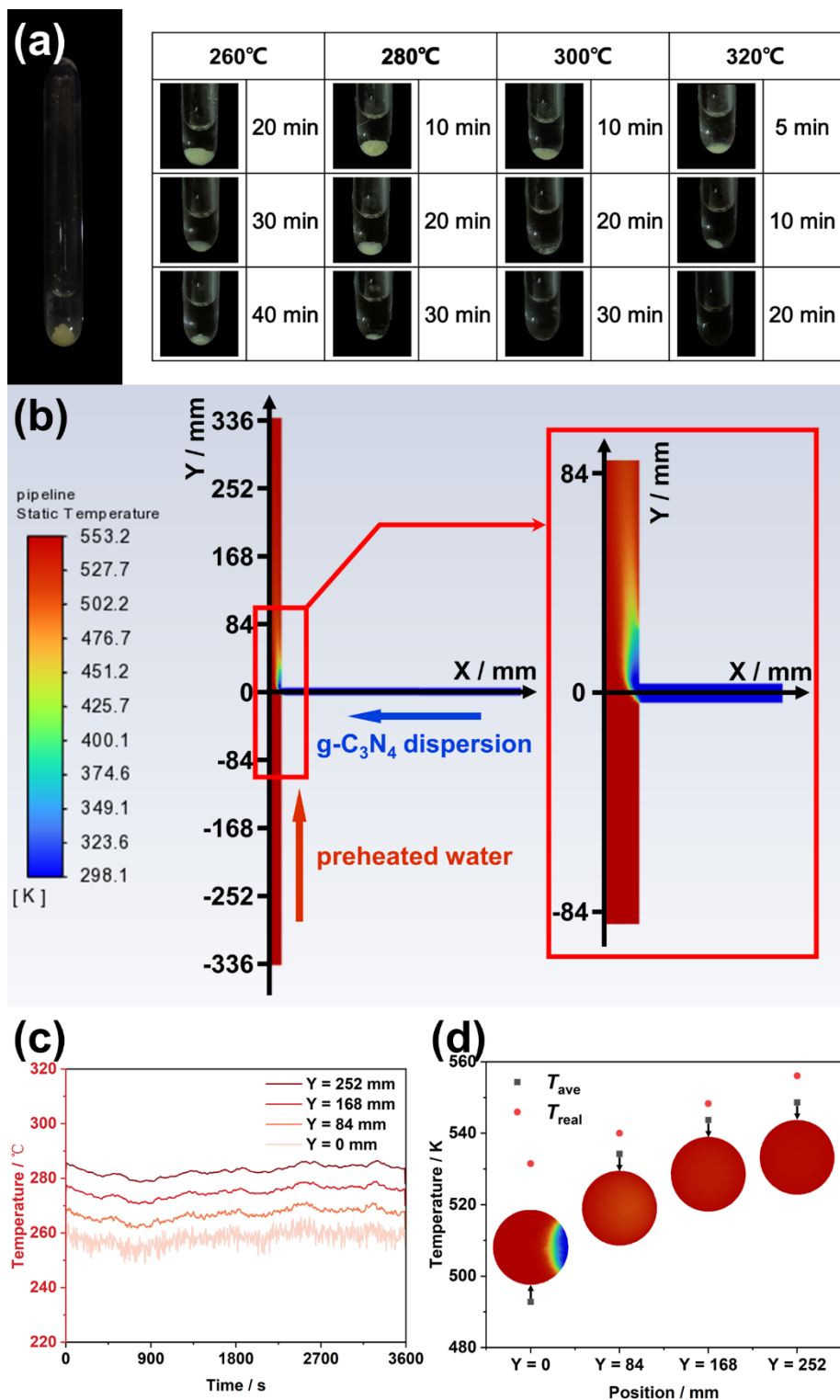
Fig. 2. (a) Visualized batch hydrothermal post treatment of g-C$_3$N$_4$ under different heating temperatures and heating time. (b) static temperature simulation of T-mixer and reactor, (c) real-time temperature curves of post-treatment process by CHS and (d) the average surface temperature calculated from static temperature simulation (T_{ave}) and the real-time temperature (T_{real}) recorded from temperature sensors in CHS.

3.1.2. Impact of temperature and residence time

As previously stated, reaction temperature and residence time were the most important parameters in hydrothermal reaction of g-C_3N_4. Accordingly, the mechanism of g-C_3N_4 hydrothermal post treatment could be effectively investigated by designing experiments about different reaction temperatures and residence time. All samples prepared in this work are shown in Table 1, and the pressure and concentration of g-C_3N_4 dispersion were fixed at 19 MPa and 5 mg mL^{-1}, respectively. In this case, CN-30/9 was prepared as a control sample at room temperature (without heating). The residence time was calculated using Eq. S1.

Table 1. Samples and corresponding experimental parameters, including experiment temperature, flow rate (m_1, m_2), residence time, yield and H_2-evolution rate.

Sample number	Sample name[a]	Condition				Result	
		Reaction temperature/°C	m_1[b] /mL min^{-1}	m_2[c] /mL min^{-1}	Residence time/s	Yield/%	H_2-evolution rate/µmol g^{-1} h^{-1}
1	CN-30/9	30	9.0	36	50.3	31.9±2	176.3±15
2	CN-260/9	260	9.0	36	50.3	13.5±2	637.3±24
3	CN-280/9	280	9.0	36	50.3	13.1±2	987.2±40
4	CN-290/9	290	9.0	36	50.3	7.3±1	769.7±28
5	CN-300/9	300	9.0	36	50.3	3.2±1	699.4±32
6	CN-300/12	300	12.0	48	37.7	3.7±1	838.7±26
7	CN-300/13.5	300	13.5	54	33.6	13.0±1	698.2±22
8	CN-300/15	300	15.0	60	30.2	18.7±2	816.4±29
9	CN-300/18	300	18.0	72	25.2	40.1±2	787.4±24

[a] The samples were designated as CN-T/m_1, where T represented the reaction temperature (°C) and [b] m_1 represented the flow rate (mL min^{-1}) of Pump (3); [c] m_2 represented the flow rate (mL min^{-1}) of Pump (4). (Error estimates of Reaction temperature, m_1 and m_2 were derived from the systematic error of the instrument, and error estimates of Yield and H_2-evolution rate were obtained based on 3 replicated experiments.)

To explore the influence of reaction temperature, the hydrothermal reactions were set at 30, 260, 280, 290 and 300°C to obtain Samples 1 to 5, respectively, while other experimental parameters were kept identical. As shown in Fig. 3a, it was observed that the H_2-evolution rates of modified photocatalysts initially increased when reaction temperature increased, but significantly decreased when reaction temperature was over 280°C. It was thus suggested that the optimum reaction temperature is 280°C, with the H_2-evolution rate of CN-280/9 5.6 times that of CN-30/9. The yield of photocatalyst continuously decreased with an increase in reaction

temperature, in line with the results of the visualized batch hydrothermal post treatment of g-C_3N_4 presented in Section 3.1.1.

To explore the influence of residence time, reaction temperature was set at 300°C with a flow rate of g-C_3N_4 dispersion (m_1) ranging from 9 to 18 mg mL^{-1} to obtain from Samples 5 to 9. The flow rate of deionized water (m_2) was fixed at four times that of m_1. The residence time of each sample is shown in Table 1. It was observed that the product yields gradually declined as the residence time increased, while the H_2-evolution rate remained relatively constant (Fig. 3b). Interestingly, compared with CN-30/9, CN-300/18 exhibited a higher yield, indicating that lots of g-C_3N_4 might settle in the pipe, but as the flow rate increased, the settling of g-C_3N_4 diminished, leading to an increase in product yield.

Photocatalytic H_2-evolution stability of CN-280/9 is shown in Fig. 3c, whereby the sacrificial agent solution was substituted by new one after each cycle. The H_2 evolution amounts of the 2nd and 3rd photocatalytic H_2-evolution cycles were 96.4% and 94.1% of the first cycle, respectively. Meanwhile, the XRD pattern of the sample after the H_2-evolution cycle test was identical to that of CN-280/9 (Fig. S2), which clearly indicated that the sample had high stability in photocatalytic H_2 evolution. Moreover, as shown in Fig. S3, the apparent quantum yields (AQYs) of CN-280/9 were 0.58%, 0.45% and 0.43% at 380 nm, 400 nm and 420 nm, respectively, which exhibited 2.3, 5.0 and 10.8 times higher at these corresponding wavelengths compared with those of CN-30/9 (0.25% at 380 nm, 0.09% at 400 nm and 0.04% at 420 nm), respectively. All of the aforementioned tests indicated that continuous hydrothermal post treatment could be a simple and effective method to improve the photocatalytic H_2-evolution activity of g-C_3N_4.
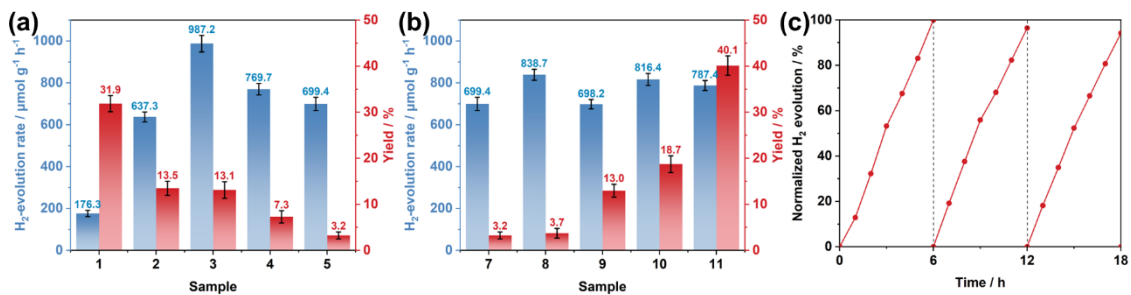

Fig. 3. (a, b) H_2-evolution rates and yields of (a) CN-T/9 (T = 30, 260, 280, 290, 300) and (b) CN-300/m_1 (m_1 = 9, 12, 13.5, 15, 18), (c) three-cycle (6 h per cycle) photocatalytic H_2-evolution stability test of CN-280/9. (Error bars were obtained based on 3 replicated experiments.)

3.2. Structural analysis and photocatalytic enhancement mechanism

While the reaction temperature was increased to 300°C, the H_2-evolution rate of CN-300/9 significantly reduced. Compared with CN-280/9 and CN-30/9, the X-ray diffraction (XRD)

11

pattern of CN-300/9 displayed the presence of some new peaks, while the typical characteristic peak of g-C_3N_4 at 12.8° disappeared (Fig. 4a) [45]. These findings indicated that a substantial structural change had taken place due to the high-temperature and high-pressure water.

Ultraviolet-visible spectrophotometer (UV-Vis) of samples are shown in Fig. 4b and Fig. 4c. The absorption capacities of long wavelength bands for samples increased with increasing reaction temperature, and decreased with decreasing residence time. Fig. 4d shows a similar result that higher reaction temperature and longer residence time leading to darker sample colors. Fig. S4 shows the band gaps of CN-30/9, CN-280/9 and CN-300/9 calculated by Kubelka-Munk function. It could be found that the hydrothermal reaction caused a large change in the band structure of g-C_3N_4 when the temperature was increased to 300°C. Combined with H_2-evolution rate in Fig. 3a and Fig. 3b, it was observed that continuous hydrothermal treatment with excessively high reaction temperature and long residence time would lead to the structural destruction of g-C_3N_4. On the contrary, appropriate reaction temperature and short residence time could moderately regulate the structure of g-C_3N_4 to a certain extent, which resulted in CN-280/9 exhibiting high photocatalytic H_2-evolution activity.
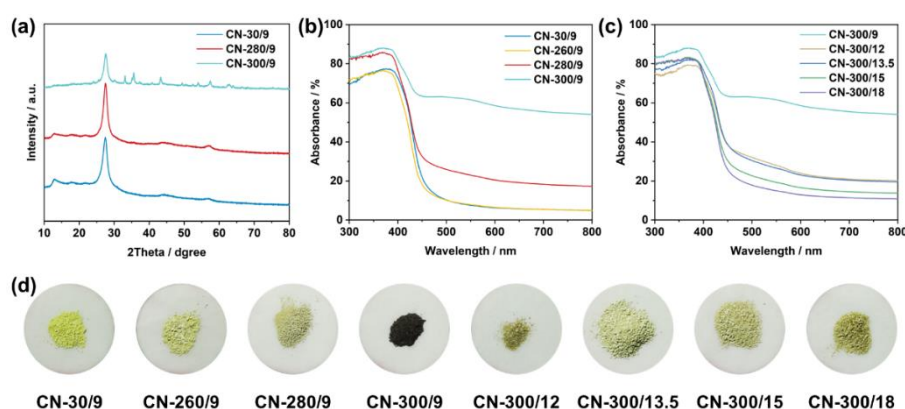

Fig. 4. (a) XRD patterns of CN-T/9 (T = 30, 280, 300), (b, c) UV-Vis of (b) CN-T/9 (T = 30, 260, 280, 300) and (c) CN-300/m_1 (m_1 = 9, 12, 13.5, 15, 18), (d) optical photographs of Samples 1 to 9.

X-ray photoelectron spectroscopy (XPS) was conducted to analyze the surface compositions and chemical states of CN-280/9 and CN-30/9. The detected elements in both samples included C, N and O, while others were absent (Fig. S5). The identical valence band maximum (VBM) position of CN-280/9 and CN-30/9 (Fig. S6) indicated the remained band structure of g-C_3N_4 after the hydrothermal post treatment under 280°C. The essential surface chemical state information was demonstrated by the results of high-resolution XPS (HRXPS) shown in Fig. 5a-5c, Table S1 and Table S2. As shown in Fig. 5a, the HRXPS of C 1s for CN-30-9 revealed

three peaks, which corresponded to the sp^2-hybridized C (N=C-N) at 288.4 eV, the C-N bond at 286.0 eV and the C-C bond at 284.8 eV, respectively [46, 47]. It was discovered that the position of C-N bond (286.3 eV) exhibited a shift to higher binding energy in CN-280/9 compared with CN-30/9. Meanwhile, the spectrum of N 1s in CN-30/9 indicated four peaks at 404.5, 401.2, 399.9 and 398.5 eV (Fig. 5b), which were attributed to the π excitation, the N-H bond, the N-C_3 in 3-s-triazine ring and the C=N-C, respectively [45, 46]. The N 1s peak associated with π excitation (404.7 eV) had experienced a shift towards higher banding energies while that associated with N-H (400.9 eV) shifted to a lower one. In addition, compared with CN-30/9, the peak-area percentages of N-H and C=N-C in CN-280/9 increased, while the peak-area percentages of π excitation and N-C_3 decreased (Table S2). The shift of the peak position and the variation of the peak-area percentages could be explained by the disruption of the 3-s-triazine ring (C_6N_7) in g-C_3N_4 by the high-temperature hydrothermal reaction and the growth of N-H at exposed N atoms. Furthermore, the limited area percentage of π-excited N in CN-280/9 suggested that the disorderly structure of CN-280/9 predominantly built a positively charged π-conjugated electronic system, while the structure containing π-π interactions was greatly reduced. This facilitated the electron transport within layer to a certain extent [17]. There are two characteristic peaks in Fig. 5c, which are the C-O bond located at 531.9 eV and the O-H bond located at 533.2 eV, respectively. The C-O bond was presented due to the incorporation of O element during the thermal polycondensation reaction of melamine in air when preparing pristine g-C_3N_4. The appearance of O-H peak was attributed to the reaction of H_2O and g-C_3N_4 during the hydrothermal process [48]. Additionally, the O 1s peak of CN-280/9 presented no obvious shift compared with CN-30/9.

Fourier transform infrared spectra (FTIR) of CN-30/9, CN-280/9 and CN-300/9 are shown in Fig. 5d, which all exhibited the peaks in the range of 1800-800 cm^{-1} due to the stretching vibrations of aromatic heptazine, but the peaks in the range of 3500-3300 cm^{-1} due to the vibrations of amino increased after hydrothermal reaction. The results of FTIR indicated that N-C_3 in g-C_3N_4 was broken due to hydrothermal reaction, and more N atoms were exposed to environment and reacted with H_2O to form the amino group, which corresponded to the results in Table S2.
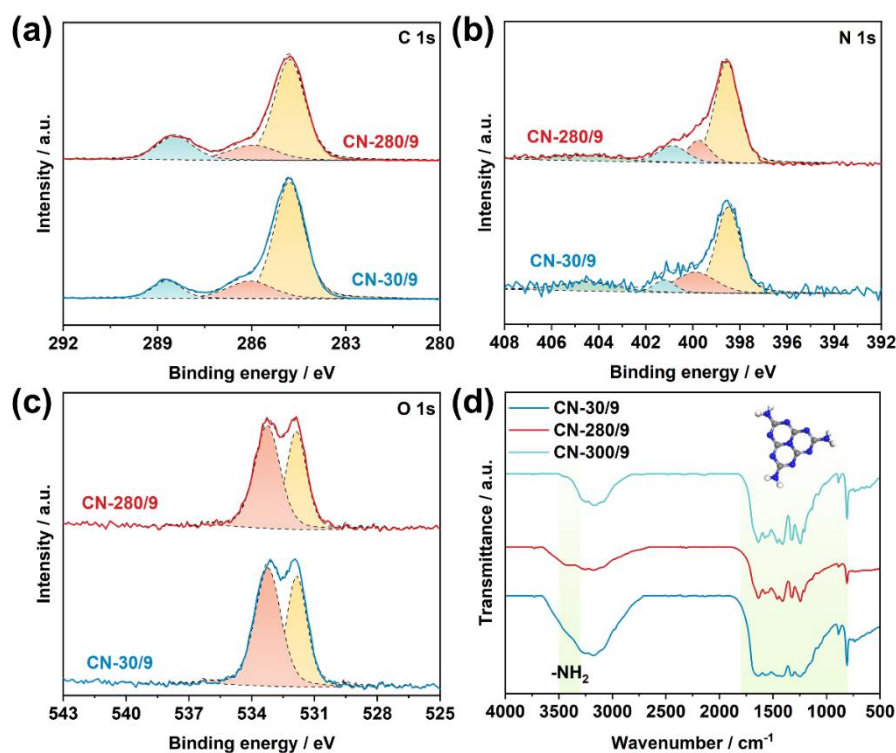
Fig. 5. (a-c) HRXPS of (a) C 1s, (b) N 1s, (c) O 1s for CN-30/9 and CN-280/9, (d) FTIR of CN-30/9 and CN-280/9.

The graphical representation in Fig. 6a shows the N_2 adsorption-desorption isotherms for CN-280/9 and CN-30/9. The specific surface area of CN-280/9 (65.8 $m^2 g^{-1}$) was 4.3 times that of CN-30/9 (15.4 $m^2 g^{-1}$), and CN-280/9 also shown higher pore volume than that of CN-30/9 (Fig. 6b), which implied a significant abundance of mesopores and micropores in CN-280/9. Additionally, the transmission electron microscopy (TEM) image of CN-30/9 (Fig. 6c) shows irregular layer stacking with a large number of pores clearly present in CN-280/9 (Fig. 6d), and the scanning electron microscopy (SEM) images (Fig. S7) show a similar pattern, which provided supplementary evidence for the large specific surface area. The increase in specific surface area led to the emergence of more active sites for photocatalytic reactions, resulting in higher H_2-evolution rate of CN-280/9.

The results of photoluminescence (PL) (Fig. 6e) and time-resolved photoluminescence (TRPL) (Fig. 6f) could reveal the migration, transfer, and recombination processes of photo-generated electron-hole pairs in semiconductors. As shown in Fig. 6e, the weaker emission intensity of CN-280/9 than that of CN-30/9 suggested the suppressed recombination of photo-generated carriers due to surface defects and porous structure after modification. Furthermore, CN-280/9 showed two emission peaks located at 458 and 445 nm, which corresponded to the blue-shift of peak at 463 nm corresponding to the quantum confinement within the nanostructured porous

14

framework of the g-C$_3$N$_4$ sheets [49, 50] and the disruption of the g-C$_3$N$_4$ structure after hydrothermal reaction, respectively. TRPL spectra (Fig. 6f) showed that the average lifetime of photo-generated carriers in CN-280/9 (2.9 ns) was less than that of CN-30/9 (3.2 ns), suggesting that the enhancement of electrons transport from bulk to surface led to the increase in photocatalytic H$_2$-evolution activity [51, 52]. This enhancement may be related to the directional movement of electrons by electrophilic groups such as hydroxyl grown on the surface of g-C$_3$N$_4$ due to hydrothermal modification [37] and the facilitated transport of electrons within layer by reduced structure containing π-π interactions in g-C$_3$N$_4$ after post-treatment. Meanwhile, the EIS Nyquist fitted plots showed that CN-280/9 had a smaller radius arc than CN-30/9 (Fig. S9), which indicated the more effective separation of photo-generated carriers of CHT-CN.
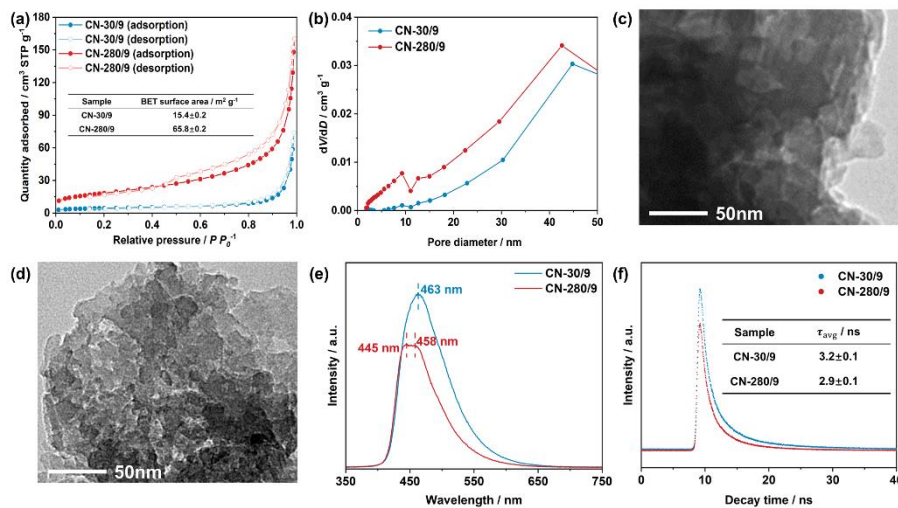
Fig. 6. (a) N$_2$ adsorption-desorption isotherms and (b) BJH pore size distribution curves of CN-30/9 and CN-280/9, (c, d) TEM images of (c) CN-30/9 and (d) CN-280/9 (scale bar: 50 nm), (e) PL spectra and (f) TRPL spectra of CN-30/9 and CN-280/9.

Based on the above tests and characterization results, it could be concluded that continuous hydrothermal treatment was an efficient g-C$_3$N$_4$ modification method, and the schematic diagram is shown in Fig. 7. During the continuous hydrothermal treatment, g-C$_3$N$_4$ photocatalyst particles, high-temperature and high-pressure liquid-phase water, water vapour and gas (CO$_2$ and NH$_3$) from partial decomposition of g-C$_3$N$_4$ formed a multiphase flow system. The high-temperature and high-pressure water facilitated the exfoliation and shearing of g-C$_3$N$_4$, leading to increased pores and enhanced specific surface area. This process also resulted in the destruction of conjugate structure in g-C$_3$N$_4$, which potentially hindered the recombination of photo-generated carriers and also enhanced the transport of electrons from bulk to surface. The state of the multiphase flow system was determined by factors including temperature, pressure,

15

382   flow rate and dispersion concentration, which had an impact on H_2-evolution rate and yield of

383   the CHT-CN.
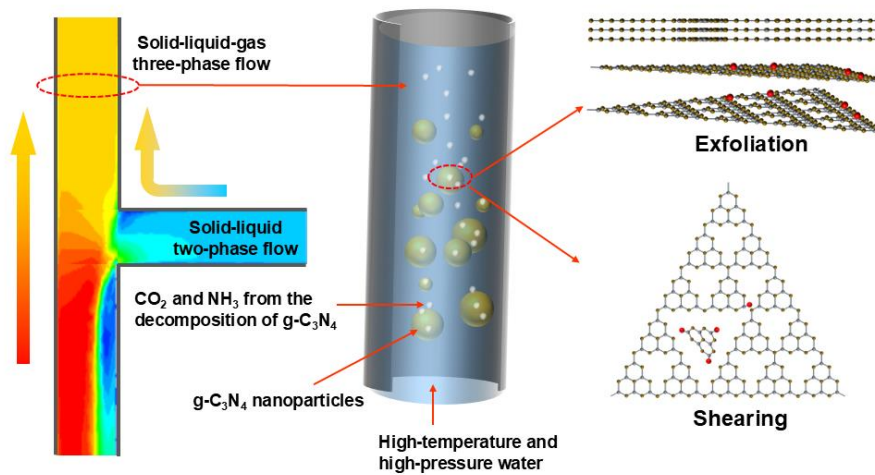
384

385   **Fig. 7.** Schematic diagram of the continuous hydrothermal post treatment of g-C_3N_4.

386

387   **4. Conclusion**

388   In this work, a mild modification of g-C_3N_4 was achieved under high-temperature hydrothermal

389   conditions using CHS, leading to the tuning of macroscopic morphology and electronic

390   structure of g-C_3N_4, while simultaneously avoiding excessive decomposition. On the one hand,

391   the continuous hydrothermal treatment significantly increased the specific surface area of g-

392   C_3N_4 and formed a porous morphology, which facilitated the increase of reactive sites. On the

393   other hand, this process also partially destroyed the triazine ring and 3-s-triazine ring structures

394   in g-C_3N_4, which hindered the recombination of photo-generated carriers and enhanced the

395   transport of electrons, and thus greatly improved the photocatalytic hydrogen production

396   performance. The modified g-C_3N_4 showed an enhanced photocatalytic H_2-evolution activity

397   about 5.6 times compared with that of CN-30/9. In addition, the continuous and uninterrupted

398   production of hydrothermal process demonstrated that continuous hydrothermal treatment

399   appeared to be a scalable strategy for preparation of photocatalysts compared to the other

400   reported methods [53, 54].

401   In the future, hydrothermal post treatment of g-C_3N_4 at higher temperatures could be explored,

402   including conditions with subcritical and supercritical water. Efforts to further increase the

403   specific surface area could be attempted by adding pore-forming agents such as H_2O_2 or NH_4Cl.

404   Optimizing the geometry of the mixer and reactor may be important to investigate the effects

405   of heat and mass transfer in g-C_3N_4 modification. Moreover, the study of the reaction

406   mechanism of hydrothermally modified g-C_3N_4 by molecular dynamics could offer valuable

407   insights and provide guidance for future research.

408

CRediT authorship contribution statement

Binjiang Zhai: Formal analysis, Investigation, Data curation, Writing – original draft. **Yi Li:** Conceptualization, Investigation, Writing – review & editing. **Yuzhou Jiang:** Formal analysis, Writing – review & editing. **Liuhao Mao:** Formal analysis, Writing – review & editing. **Jinwen Shi:** Conceptualization, Formal analysis, Writing – review & editing, Supervision, Project administration. **Qiangqiang Zhao:** Software. **Zhongda Bin:** Writing – review & editing. **Fanyu Wang:** Writing – review & editing. **Yanping Du:** Conceptualization, Formal analysis, Writing – review & editing. **Hui Jin:** Conceptualization, Writing – review & editing, Supervision.

Declaration of competing interest

The authors declare that they have no known competing financial interests or personal relationships that could have appeared to influence the work reported in this paper.

Supporting Information

Supporting Information is available from the Wiley Online Library or from the author.

Appendix A. Supplementary data

The Supplementary data to this article was in the single file named as "Supporting Information".

Data availability

Data will be made available on request.

References

[1] A. Fujishima, K. Honda, Electrochemical photolysis of water at a semiconductor electrode, Nature 238 (1972) 37-38, https://doi.org/10.1038/238037a0.

[2] P.S. Basavarajappa, S.B. Patil, N. Ganganagappa, K.R. Reddy, A.V. Raghu, C.V. Reddy, Recent progress in metal-doped TiO_2, non-metal doped/codoped TiO_2 and TiO_2 nanostructured hybrids for enhanced photocatalysis, Int. J. Hydrogen Energ. 45 (2020) 7764-7778, https://doi.org/10.1016/j.ijhydene.2019.07.241.

[3] J.L. Li, H. Chang, S.L. Feng, H.R. Jian, Q.Q. Shen, X.G. Liu, H.S. Jia, J.B. Xue, TiO_2@Ti MOFs hollow double-shell structure by in-situ self-sacrificial hydrolytic etching for enhanced photocatalytic hydrogen evolution, Chem. Eng. J. 498 (2024) 11, https://doi.org/10.1016/j.cej.2024.155542.

[4] L. Pan, T. Muhammad, L. Ma, Z.-F. Huang, S. Wang, L. Wang, J.J. Zou, X. Zhang, MOF-derived C-doped ZnO prepared via a two-step calcination for efficient photocatalysis, Appl. Catal. B-Environ. 189 (2016) 181-191, https://doi.org/10.1016/j.apcatb.2016.02.066.

[5] C.H. Shen, Y. Chen, X.J. Xu, X.Y. Li, X.J. Wen, Z.T. Liu, R. Xing, H. Guo, Z.H. Fei, Efficient photocatalytic H_2 evolution and Cr(VI) reduction under visible light using a novel Z-scheme $SnIn_4S_8$/CeO_2 heterojunction photocatalysts, J. Hazard. Mater. 416 (2021) 126217, https://doi.org/10.1016/j.jhazmat.2021.126217.

[6] Z.L. Ma, L. Xu, K.J. Dong, T. Chen, S.X. Xiong, B.J. Peng, J. Zeng, S.H. Tang, H.T. Li, X. Huang, K.W. Luo, L.L. Wang, GaN/Surface-modified graphitic carbon nitride heterojunction: Promising photocatalytic hydrogen evolution materials, Int. J. Hydrogen Energ. 47 (2022) 7202-7213, https://doi.org/10.1016/j.ijhydene.2019.07.241.

[7] J. Liao, B. Sa, J. Zhou, R. Ahuja, Z. Sun, Design of High-Efficiency Visible-Light Photocatalysts for water splitting: MoS_2/AlN(GaN) heterostructures, J. Phys. Chem. C 118 (2014) 17594-17599, https://doi.org/10.1021/jp5038014.

[8] Y.X. Chen, W. Zhong, F. Chen, P. Wang, J.J. Fan, H.G. Yu, Photoinduced self-stability mechanism of CdS photocatalyst: The dependence of photocorrosion and H_2-evolution performance, J. Mater. Sci. Technol. 121 (2022) 19-27, https://doi.org/10.1016/j.jmst.2021.12.051.

[9] J. Yang, H. Yan, X. Wang, F. Wen, Z. Wang, D. Fan, J. Shi, C. Li, Roles of cocatalysts in Pt-PdS/CdS with exceptionally high quantum efficiency for photocatalytic hydrogen production, J. Catal. 290 (2012) 151-157, https://doi.org/10.1016/j.jcat.2012.03.008.

[10] J. Shi, Y. Zhang, Y. Hu, X. Guan, Z. Zhou, L. Guo, NH_3-treated MoS_2 nanosheets as photocatalysts for enhanced H_2 evolution under visible-light irradiation, J. Alloys Compd. 688

475 (2016) 368-375, https://doi.org/10.1016/j.jallcom.2016.07.053.

476 [11] C. Cai, Z. Wang, J. Shi, Y. Zhang, L. Mao, F. Chen, T. Wang, Y. Chen, Facile one-pot

477 pyrolysis preparation of SnO_2/g-C_3N_4 composites for improved photocatalytic H_2 production,

478 J. Chem. Technol. Biotechnol. 97 (2022) 2921-2931, https://doi.org/10.1002/jctb.7167.

479 [12] Y. Liu, W. Miao, Z. Chen, D.C. Yao, J.G. Wang, X.Y. Chen, S. Mao, Enhanced hydrogen

480 peroxide production under visible light via pyrimidine and glucose polymer modified graphitic

481 carbon nitride in pure water, Chem. Eng. J. 496 (2024) 7,

482 https://doi.org/10.1016/j.cej.2024.153871.

483 [13] R.F. Chen, Y. Wang, Y. Ma, A. Mal, X.Y. Gao, L. Gao, L.J. Qiao, X.B. Li, L.Z. Wu, C.

484 Wang, Rational design of isostructural 2D porphyrin-based covalent organic frameworks for

485 tunable photocatalytic hydrogen evolution, Nat. Commun. 12 (2021),

486 https://doi.org/10.1038/s41467-021-21527-3.

487 [14] Y. Wang, Y. Deng, H. Xia, R.Z. Zhang, J. Liu, H.X. Zhang, Y.J. Sun, Z. Zhang, X.Q. Lu,

488 Superhydrophilic triazine-based covalent organic frameworks via post-modification of FeOOH

489 clusters for boosted photocatalytic performance, Small Methods 8 (2024) 10,

490 https://doi.org/10.1002/smtd.202300163.

491 [15] X. Wang, K. Maeda, A. Thomas, K. Takanabe, G. Xin, J.M. Carlsson, K. Domen, M.

492 Antonietti, A metal-free polymeric photocatalyst for hydrogen production from water under

493 visible light, Nat. Mater. 8 (2009) 76-80, https://doi.org/10.1038/nmat2317.

494 [16] S. Cao, J. Yu, g-C_3N_4-based photocatalysts for hydrogen generation, J. Phys. Chem. Lett.

495 5 (2014) 2101-2107, https://doi.org/10.1021/jz500546b.

496 [17] W.J. Ong, L.L. Tan, Y.H. Ng, S.T. Yong, S.P. Chai, Graphitic carbon nitride (g-C_3N_4)-based

497 photocatalysts for artificial photosynthesis and environmental remediation: Are we a step closer

498 to achieving sustainability? Chem. Rev. 116 (2016) 7159-7329,

499 https://doi.org/10.1021/acs.chemrev.6b00075.

500 [18] Y. Yu, Q. Jin, D. Zhu, Y. Ren, Exceptional Lithium-Ion Storage Performance on an azo-

501 bridged covalent heptazine framework, Adv. Funct. Mater. 34 (2023) 2308706,

502 https://doi.org/10.1002/adfm.202308706.

503 [19] K. Schwinghammer, M.B. Mesch, V. Duppel, C. Ziegler, J. Senker, B.V. Lotsch,

504 Crystalline carbon nitride nanosheets for improved visible-light hydrogen evolution, J. Am.

505 Chem. Soc. 136 (2014) 1730-1733, https://doi.org/10.1021/ja411321s.

506 [20] W. Liu, J. Shen, X.F. Yang, Q.Q. Liu, H. Tang, Dual Z-scheme g-C_3N_4/Ag_3PO_4/Ag_2MoO_4

507 ternary composite photocatalyst for solar oxygen evolution from water splitting, Appl. Surf. Sci.

508 456 (2018) 369-378, https://doi.org/10.1016/j.apsusc.2018.06.156.

509   [21] P. Niu, L.L. Zhang, G. Liu, H.M. Cheng, Graphene-like carbon nitride nanosheets for

510   improved photocatalytic activities, Adv. Funct. Mater. 22 (2012) 4763-4770,

511   https://doi.org/10.1002/adfm.201200922.

512   [22] J.W. Seo, Y.W. Jun, S.W. Park, H. Nah, T. Moon, B. Park, J.G. Kim, Y.J. Kim, J. Cheon,

513   Two-dimensional nanosheet crystals, Angew. Chem. Int. Ed. 46 (2007) 8828-8831,

514   https://doi.org/10.1002/anie.200703175.

515   [23] L.J. Hu, Y.M. Du, R. Liu, S.S. Yang, H.L. Tang, X.Z. Yin, Q.X. Xiao, X.K. Wang, H.Q.

516   Wang, Alkali metal cation adsorption-induced surface polarization in polymeric carbon nitride

517   for enhanced photocatalytic hydrogen peroxide production, J. Colloid Interface Sci. 679 (2025)

518   456-464, https://doi.org/10.1016/j.jcis.2024.10.004.

519   [24] X.C. Hao, X.L. Ji, Q. Zhang, Effective improvement of the photocatalytic efficiency of g-

520   C_3N_4 by a green hydrothermal treatment method, Mater. Lett. 185 (2016) 29-31,

521   https://doi.org/10.1016/j.matlet.2016.08.097.

522   [25] Z.Y. Mao, J.J. Chen, Y.F. Yang, L.J. Bie, B.D. Fahlman, D.J. Wang, Modification of surface

523   properties and enhancement of photocatalytic performance for g-C_3N_4 via plasma treatment,

524   Carbon 123 (2017) 651-659, https://doi.org/10.1016/j.carbon.2017.08.020.

525   [26] H.Y. Tian, X. Liu, Z.Q. Liang, P.Y. Qiu, X. Qian, H.Z. Cui, J. Tian, Gold nanorods/g-C_3N_4

526   heterostructures for plasmon-enhanced photocatalytic H_2 evolution in visible and near-infrared

527   light, J. Colloid Interface Sci., 557 (2019) 700-708, https://doi.org/ 10.1016/j.jcis.2019.09.075.

528   [27] S. Guo, Z. Deng, M. Li, B. Jiang, C. Tian, Q. Pan, H. Fu, Phosphorus-doped carbon nitride

529   tubes with a layered micro-nanostructure for enhanced visible-light photocatalytic hydrogen

530   evolution, Angew. Chem. Int. Ed. 55 (2016) 1830-1834,

531   https://doi.org/10.1002/anie.201508505.

532   [28] S. Zhang, J. Chen, C. Fang, Y. Zhang, Z. Xu, Z. Yan, K. Yao, Enhanced photocatalytic

533   removal of antibiotics over graphitic carbon nitride induced by acetic acid post-treatment,

534   Colloids Surf. 664 (2023) 131165, https://doi.org/10.1016/j.colsurfa.2023.131165.

535   [29] A. Beyhaqi, S.M.T. Azimi, Z. Chen, C. Hu, Q. Zeng, Exfoliated and plicated g-C_3N_4

536   nanosheets for efficient photocatalytic organic degradation and hydrogen evolution, Int. J.

537   Hydrogen Energ. 46 (2021) 20547-20559, https://doi.org/10.1016/j.ijhydene.2021.03.174.

538   [30] H. Nie, M. Ou, Q. Zhong, S. Zhang, L. Yu, Efficient visible-light photocatalytic oxidation

539   of gaseous NO with graphitic carbon nitride (g-C_3N_4) activated by the alkaline hydrothermal

540   treatment and mechanism analysis, J. Hazard. Mater. 300 (2015) 598-606,

541   https://doi.org/10.1016/j.jhazmat.2015.07.066.

542   [31] T. Sano, S. Tsutsui, K. Koike, T. Hirakawa, Y. Teramoto, N. Negishi, K. Takeuchi,

Activation of graphitic carbon nitride (g-C_3N_4) by alkaline hydrothermal treatment for photocatalytic NO oxidation in gas phase, J. Mater. Chem. A 1 (2013) 6489-6496, https://doi.org/10.1039/c3ta10472a.

[32] Y. Zhang, J. Shi, Z. Huang, X. Guan, S. Zong, C. Cheng, B. Zheng, L. Guo, Synchronous construction of CoS_2 in-situ loading and S doping for g-C_3N_4: Enhanced photocatalytic H_2-evolution activity and mechanism insight, Chem. Eng. J. 401 (2020), https://doi.org/10.1016/j.cej.2020.126135.

[33] H. Huang, K. Xiao, N. Tian, F. Dong, T. Zhang, X. Du, Y. Zhang, Template-free precursor-surface-etching route to porous, thin g-C_3N_4 nanosheets for enhancing photocatalytic reduction and oxidation activity, J. Mater. Chem. A 5 (2017) 17452-17463, https://doi.org/10.1039/c7ta04639a.

[34] Z.Y. Gu, Z.T. Cui, Z.J. Wang, K.S. Qin, Y. Asakura, T. Hasegawa, S. Tsukuda, K. Hongo, R. Maezono, S. Yin, Carbon vacancies and hydroxyls in graphitic carbon nitride: Promoted photocatalytic NO removal activity and mechanism, Appl. Catal. B-Environ. 279 (2020) 119376, https://doi.org/10.1016/j.apcatb.2020.119376.

[35] S.X. Yu, J.Y. Li, Y.H. Zhang, M. Li, F. Dong, T.R. Zhang, H.W. Huang, Local spatial charge separation and proton activation induced by surface hydroxylation promoting photocatalytic hydrogen evolution of polymeric carbon nitride, Nano Energy, 50 (2018) 383-392, https://doi.org/10.1016/j.nanoen.2018.05.053.

[36] B.C. Wang, L.L. Huang, T. Peng, R. Wang, J. Jin, H.W. Wang, B.B. He, Y.S. Gong, Attapulgite-intercalated g-C_3N_4/$ZnIn_2S_4$ 3D hierarchical Z-scheme heterojunction for boosting photocatalytic hydrogen production, J. Colloid Interface Sci. 675 (2024) 52-63, https://doi.org/10.1016/j.jcis.2024.06.243.

[37] L. Mao, B. Lu, J. Shi, Y. Zhang, X. Kang, Y. Chen, H. Jin, L. Guo, Rapid high-temperature hydrothermal post treatment on graphitic carbon nitride for enhanced photocatalytic H_2 evolution, Catal. Today, 409 (2022) 4-102, https://doi.org/10.1016/j.cattod.2022.03.035.

[38] L. Mao, B. Zhai, J. Shi, X. Kang, B. Lu, Y. Liu, C. Cheng, H. Jin, E. Lichtfouse, L. Guo, Supercritical CH_3OH-triggered isotype heterojunction and groups in g-C_3N_4 for enhanced photocatalytic H_2 3volution, ACS Nano, 18 (2024) 13939-13949, https://doi.org/10.1021/acsnano.4c03922.

[39] S. Ohara, T. Mousavand, T. Sasaki, M. Umetsu, T. Naka, T. Adschiri, Continuous production of fine zinc oxide nanorods by hydrothermal synthesis in supercritical water, J. Mater. Sci. 43 (2008) 2393-2396, https://doi.org/10.1007/s10853-007-1823-3.

[40] T. Sasaki, S. Ohara, T. Naka, J. Vejpravova, V. Sechovsky, M. Umetsu, S. Takami, B.

Jeyadevan, T. Adschiri, Continuous synthesis of fine $MgFe_2O_4$ nanoparticles by supercritical hydrothermal reaction, J. Supercrit. Fluid, 53 (2010) 92-94, https://doi.org/10.1016/j.supflu.2009.11.005.

[41] P. Boldrin, A.K. Hebb, A.A. Chaudhry, L. Otley, B. Thiebaut, P. Bishop, J.A. Darr, Direct synthesis of nanosized $NiCo_2O_4$ spinel and related compounds via continuous hydrothermal synthesis methods, Ind. Eng. Chem. Res. 46 (2007) 4830-4838, https://doi.org/10.1021/ie061396b.

[42] L. Guo, Z. Ou, Y. Liu, Z. Ge, H. Jin, G. Ou, M. Song, Z. Jiao, W. Jing, Technological innovations on direct carbon mitigation by ordered energy conversion and full resource utilization, Carbon Neutrality, 1 (2022) 4, https://doi.org/10.1007/s43979-022-00009-5.

[43] L.J. Guo, H. Jin, Z.W. Ge, Y.J. Lu, C.Q. Cao, Industrialization prospects for hydrogen production by coal gasification in supercritical water and novel thermodynamic cycle power generation system with no pollution emission, Sci. China Technol. Sc. 58 (2015) 1989-2002, https://doi.org/10.1007/s11431-015-5967-0.

[44] E. Lester, P.J. Blood, J.P. Denyer, B.J. Azzopardi, J. Li, M. Poliakoff, Impact of reactor geometry on continuous hydrothermal synthesis mixing, Mater. Res. Innov. 14 (2010) 19-26, https://doi.org/10.1179/143307510x12599329343042.

[45] C. Cheng, L. Mao, Z. Huang, J. Shi, B. Zheng, Y. Zhang, L. Guo, Bridging regulation in graphitic carbon nitride for band-structure modulation and directional charge transfer towards efficient H_2 evolution under visible-light irradiation, J. Colloid Interface Sci. 601 (2021) 220-228, https://doi.org/10.1016/j.jcis.2021.05.109.

[46] X. Fang, R. Gao, Y. Yang, D. Yan, A cocrystal precursor strategy for carbon-rich graphitic carbon nitride toward high-efficiency photocatalytic overall water splitting, iScience 16 (2019) 22-30, https://doi.org/10.1016/j.isci.2019.05.015.

[47] F. Xue, Y. Si, M. Wang, M. Liu, L. Guo, Toward efficient photocatalytic pure water splitting for simultaneous H_2 and H_2O_2 production, Nano Energy, 62 (2019) 823-831, https://doi.org/10.1016/j.nanoen.2019.05.086.

[48] J. Li, B. Shen, Z. Hong, B. Lin, B. Gao, Y. Chen, A facile approach to synthesize novel oxygen-doped g-C_3N_4 with superior visible-light photoreactivity, ChemComm. 48 (2012) 12017-12019, https://doi.org/10.1039/c2cc35862j.

[49] Q. Han, B. Wang, J. Gao, Z. Cheng, Y. Zhao, Z. Zhang, L. Qu, Atomically Thin mesoporous nanomesh of graphitic C_3N_4 for high-efficiency photocatalytic hydrogen evolution, ACS Nano, 10 (2016) 2745-2751, https://doi.org/10.1021/acsnano.5b07831.

[50] Y. Cui, J. Zhang, G. Zhang, J. Huang, P. Liu, M. Antonietti, X. Wang, Synthesis of bulk

and nanoporous carbon nitride polymers from ammonium thiocyanate for photocatalytic hydrogen evolution, J. Mater. Chem. 21 (2011) 13032, https://doi.org/10.1039/c1jm11961c.

[51] W. Tu, Y. Zhou, Q. Liu, S. Yan, S. Bao, X. Wang, M. Xiao, Z. Zou, An in situ simultaneous reduction-hydrolysis technique for fabrication of TiO_2-graphene 2D sandwich-like hybrid nanosheets: Graphene-promoted selectivity of photocatalytic-driven hydrogenation and coupling of CO_2 into methane and ethane, Adv. Funct. Mater. 23 (2013) 1743-1749, https://doi.org/10.1002/adfm.201202349.

[52] J. Fu, B. Zhu, C. Jiang, B. Cheng, W. You, J. Yu, Hierarchical porous O-doped g-C_3N_4 with enhanced photocatalytic CO_2 reduction activity, Small 13 (2017) 1603938, https://doi.org/10.1002/smll.201603938.

[53] J. Wang, S. Wang, A critical review on graphitic carbon nitride (g-C_3N_4)-based materials: preparation, modification and environmental application, Coordin. Chem.y Rev. 453 (2022) 214338, https://doi.org/10.1016/j.ccr.2021.214338.

[54] X. Song, L. Chen, L. Gao, J. Ren, Z. Yuan, Engineering g-C_3N_4 based materials for advanced photocatalysis: recent advances, Green Energy Environ. 9 (2024) 166-197, https://doi.org/10.1016/j.gee.2022.12.005.